sealing with coverslips, and this was subsequently filled with 100 mM sucrose solution. To begin generating vesicles from the film, we applied an alternating electric field to the electrodes (10 Hz, 10 V) while the chamber was mounted and viewed on the stage of an inverted microscope. Giant vesicles attached to the film-coated electrode were visible after 15 to 60 min. These were dissociated from the electrodes by lowering the frequency to 3 to 5 Hz for at least 15 min. The electroformation method is adapted from that of M. I. Angelova, S. Soleau, P. Meleard, J. F. Faucon, and P. Bothorel [*Prog. Coll. Polm. Sci.* **89**, 127 (1992)], as previously used by M. L. Longo, A. J. Waring, and D. A. Hammer [*Biophys. J.* **73**, 1430 (1997)]. The vesicles were stable for at least several days when kept sealed from air in a gas-tight, plastic syringe. Of additional note, vesicles were stable when resuspended in physiological saline at temperatures ranging from 10° to 50°C. Micromanipulation was done with micropipette systems analogous to those described by M. L. Longo *et al.* and D. E. Discher, N. Mohandas, and E. A. Evans [*Science* **266**, 1032 (1994)].

11. E. Evans and W. Rawicz, *Phys. Rev. Lett.* **64**, 2094 (1990); W. Helfrich and R.-M. Servuss, *Nuovo Cimento* **D3**, 137 (1984). Note that K_a did not differ by more than 10 to 20% from its nonrenormalized value.

12. J. Israelachvili, *Intermolecular and Surface Forces* (Academic Press, New York, ed. 2, 1991).

13. E. Evans and D. Needham, *J. Phys. Chem.* **91**, 4219 (1987).

14. I. Szleifer, D. Kramer, A. Ben-Shaul, D. Roux, W. M. Gelbart, *Phys. Rev. Lett.* **60**, 1966 (1988); A. Ben-Shaul, in (*3*), chap. 7.

15. A. G. Petrov and J. Bivas, *Prog. Surf. Sci.* **18**, 359 (1984).

16. R. R. Netz and M. Schick, *Phys. Rev. E* **53**, 3875 (1996). In this reference, the self-consistent calculation models lipids as nearly symmetric diblock copolymers, which are clearly closer in form to the molecules of this study.

17. D. Needham and R. S. Nunn, *Biophys. J.* **58**, 997 (1990).

18. Because the average interfacial area per chain, $<A_c>$, in the lamellar state has been estimated to be $<A_c> \gtrsim 2.5$ nm^2 per molecule, one estimates that $E_c \gtrsim 1.3$ $k_B T$.

19. Vesicles were prepared in 100 mOsm sucrose solution, which established an initial, internal osmolarity. They were then suspended in an open-edge chamber formed between cover slips and containing 100 mOsm glucose. A single vesicle was aspirated with a suction pressure sufficient to smooth membrane fluctuations; the pressure was then lowered to a small holding pressure. With a second, transfer pipette, the vesicle was moved to a second chamber with 120 mOsm glucose. Water flows out of the vesicle due to the osmotic gradient between inside and outside, which leads to an increased projection length that is monitored over time. The exponential decrease in vesicle volume was calculated from video images and then fit to determine the permeability coefficient (P_f) (*4*). For reference, $P_f = 23.5 \pm 1.7$ μm/s for SOPC from this method.

20. H. J. Deuling and W. Helfrich, *J. Phys.* **37**, 1335 (1976); S. Svetina and B. Zeks, *Eur. Biophys.* **17**, 101 (1989); U. Seifert, K. Berndl, R. Lipowsky, *Phys. Rev. A* **44**, 1182 (1991).

21. U. Seifert and R. Lipowsky, in (*3*), chap. 8; H.-G. Dobreiner, E. Evans, M. Kraus, U. Seifert, M. Wortis, *Phys. Rev. E* **55**, 4458 (1997).

22. S. Chaieb and S. Rica, *Phys. Rev. E* **58**, 7733 (1998).

23. We thank E. A. Evans, D. Needham, P. Nelson, and T. Lubensky for discussions. Support was primarily provided by the NSF-supported Materials Research Science and Engineering Center (MRSEC) at the University of Pennsylvania (DMR96-32598) and both the Center for Interfacial Engineering (CIE) and the MRSEC (DMR 98-09364) at the University of Minnesota. The work was also supported in part by grants from the Whitaker Foundation (D.D.) and National Institutes of Health [R01-HL62352-01(D.D.) and P01-HLI8208 (D.H.)].

27 January 1999; accepted 5 April 1999

The Formation of Jupiter's Faint Rings

Joseph A. Burns,[1]* Mark R. Showalter,[2] Douglas P. Hamilton,[3] Philip D. Nicholson,[1] Imke de Pater,[4] Maureen E. Ockert-Bell,[1] Peter C. Thomas[1]

Observations by the Galileo spacecraft and the Keck telescope showed that Jupiter's outermost (gossamer) ring is actually two rings circumscribed by the orbits of the small satellites Amalthea and Thebe. The gossamer rings' unique morphology—especially the rectangular end profiles at the satellite's orbit and the enhanced intensities along the top and bottom edges of the rings—can be explained by collisional ejecta lost from the inclined satellites. The ejecta evolves inward under Poynting-Robertson drag. This mechanism may also explain the origin of Jupiter's main ring and suggests that faint rings may accompany all small inner satellites of the other jovian planets.

The well-known, opaque rings of Saturn and Uranus are populated primarily by centimeter- to meter-sized particles. In addition, all four giant planets have extensive but much more tenuous rings (*1*, *2*) containing mainly micrometer-sized particles. Because particle collisions are unimportant in such rarified systems and because small grains are substantially perturbed by nongravitational forces, these ethereal rings provide valuable dynamical counterpoints to the dense, collisionally dominated systems.

Jupiter's rings—the archetype of ethereal ring systems—have three components (*3*): a main ring, an inner halo, and an outer gossamer ring. The main ring of normal optical depth $\tau \sim 10^{-6}$ and thickness <30 km extends radially inward about 6000 km (jovian radius = 71,398 km) from the orbit of the tiny moon Adrastea, with a dip in brightness of 20 to 30% around Metis's orbit (Table 1). Immediately interior to the main ring is the halo, a $\sim 10^4$-km-thick and $\sim 2 \times 10^4$-km-wide torus of dust, with τ comparable to the main ring. Exterior to the main ring lies the broad, fainter gossamer ring, with $\tau \sim 10^{-7}$, whose inner portion was observed in one Voyager image (*4*).

The ring system's structure was confirmed and refined through images obtained by the Galileo spacecraft (*5*) and the Keck 10-m telescope (*6*). The gossamer ring is actually two distinct, fairly uniform rings (Fig. 1, A and B). The brighter and narrower (Amalthea) ring is visible stretching radially outward from the main ring to the satellite Amalthea's orbit at 181,350 km. The fainter

and wider (Thebe) ring is terminated at the satellite Thebe's orbit (221,900 km). Some very diffuse material, which we refer to as the exterior gossamer material, seems to reach past Thebe, to perhaps 265,000 km.

As seen in these almost edge-on images, Jupiter's gossamer rings have a unique form. At their ansae, both rings have cross sections that are approximately rectangular, unlike the elliptical ends typically noted in images of thin, flat equatorial rings. As measured near the ansae, the half-thicknesses T of the gossamer rings are ~ 1300 km [inclination (i) = 0.41°] for the Amalthea ring and ~ 4400 km ($i = 1.14°$) for the Thebe ring, with uncertainties of ± 100 km ($\pm 0.03°$). These values are similar to the maximum excursions of the satellites associated with these rings from Jupiter's equatorial plane [1160 and 4310 km, respectively, with errors of ± 150 km (*7*)]. In addition, the radial excursions of the source satellites, as defined by their orbital eccentricities, seem to determine the radial decrease in brightness at the ansae of both rings (see crosses in Fig. 1A).

The ring's upper and lower edges are much brighter than their central cores (Fig. 1A), suggesting that the ring material is concentrated near the edges. Furthermore, the height (off the equatorial plane) of the peak brightness in each gossamer ring decreases linearly with projected radius as does the ring's total vertical extent in backscattered light (*6*). A similar banded appearance was inferred for the distribution of interplanetary dust particles (IDPs) from Infrared Astronomical Satellite scans of the zodiacal light (*8*). The cause is likely the same: a swarm of orbiting particles, with similar inclinations but random node orientations, that spend more time at their vertical turning points above and below the ecliptic (interplanetary case) or equatorial (jovian case) plane.

In the Voyager discovery image (*4*) and in two early Galileo frames (*5*), the Amalthea ring brightens by tens of percent with smaller scat-

[1]Center for Radiophysics and Space Research, Cornell University, Ithaca, NY 14853, USA. [2]Space, Telecommunications and Radioscience Laboratory, Stanford University, Stanford, CA 94305, USA. [3]Department of Astronomy, University of Maryland, College Park, MD 20742, USA. [4]Department of Astronomy, University of California, Berkeley, CA 94720, USA.

*To whom correspondence should be addressed. E-mail: jab16@cornell.edu

tering angles θ, suggesting the photometric dominance of micrometer-sized grains (9). To estimate the phase brightening of Amalthea ring particles, we removed a modeled Thebe ring contribution and then derived the Amalthea ring's vertically integrated brightness profile from edge-on image 41660888922. We next divided that curve through by the Amalthea ring's expected profile, where we consider the ring brightness to vary only because of the changing line of sight (LOS) through a model ring, in which grains leave the source satellite and drift inward at a uniform rate (see below and Fig. 2). Relative to the expected profile, the Amalthea ring brightens by an additional factor of 1.3 as θ decreases from 1.5° to 1.2°. We attribute this increase to the intrinsic phase function of the ring grains. For comparison, this relative-brightness factor would be unity for 1-μm dust, 2.5 for 10-μm particles, and about 2 for 50-μm grains (10). Our measurement is consistent with the Amalthea ring dust being dominantly composed of particles having a radius of 5 μm. Although such grains dominate in the Galileo viewing geometry, many other grain sizes may be present.

The rate at which mass, M_i, is supplied to a ring in time t due to impacts at speed v on an isolated satellite of radius R_i is

$$dM_i/dt \sim \Phi_i\, Y F_e R_i^2 \qquad (1)$$

where Φ_i is the mass flux density of hypervelocity impactors, Y is the impact yield (the ratio of ejected mass to projectile mass), and F_e is the fraction of impact ejecta that is moving swiftly enough to escape the satellite. Y depends on the projectile's specific kinetic energy and is on the order of $10v^2$ for v in units of kilometers per second (11). Φ_i increases close to Jupiter where gravitational focusing causes collisions to be more frequent and more energetic, elevating yields for similarly sized impactors. On the basis of empirical fits to hypervelocity-cratering experiments, the fractional mass ejected above speed $v \sim (v_{crit}/v)^{9/4}$, where v_{crit}, the minimum speed at which impact ejecta is launched, is typically 10 to 100 m s^{-1}, depending on the regolith's nature (1). For an isolated satellite, the escape speed $v_{esc} \propto R_i$ and is ~10 to 100 m s^{-1} for spheres the size of the jovian ring satellites (Table 1). Hence, $F_e \propto R_i^{-9/4}$ and $dM_i/dt \propto R_i^{-1/4}$ if $v_{crit} < v_{esc}$. Thus, counterintuitively, smaller moons provide more escaped ejecta than larger moons do. The optimum source has a radius such that its $v_{esc} = v_{crit}$; for a soft regolith and a density of 2 g cm^{-3}, this radius is 5 to 10 km, like that of Adrastea.

Because some of the ring moons reside within Jupiter's Roche zone, the loss of impact ejecta will be accentuated [(12); figure 4 in (13)]. We computed the speeds at which ejecta launched at ±45° from the local ver-

tical will escape the jovian ring moons from four equatorial surface locations (leading, Jupiter-facing, trailing, and anti-Jupiter) for homogeneous, rotationally locked satellites whose shapes have been measured (14). In all cases, v_{esc} was greatly decreased across most of the satellite's surface, because of tidal effects and nonsphericity (see Table 1). The effect is largest for the closer-in moons, even vanishing over portions of Adrastea. Including these variations in v_{esc}, dM_i/dt is about the same for Thebe and Amalthea, larger for Metis, and greatest for tiny Adrastea.

Because the gossamer rings reside deep within Jupiter's gravity well and within the lethal jovian magnetosphere, their microme-

ter-sized grains are rapidly destroyed or swiftly removed from the system. Lifetimes for 1-μm particles have been estimated as 10^2 to 10^4 years for erosion by sputtering and 10^4 to 10^6 years for catastrophic fragmentation after micrometeoroid bombardment (1, 13).

Circumjovian dust grains evolve orbitally by several processes. Poynting-Robertson (P-R) drag, due to momentum transferred from absorbed solar radiation, induces orbits to spiral inward over the Poynting-Robertson time $T_{P-R} = 10^5 r$ years, where r is the particle radius in micrometers. Plasma drag, which pushes grains away from the synchronous orbital radius R_{syn} (15), was estimated to have a characteristic time scale of (20 to 2000)r years
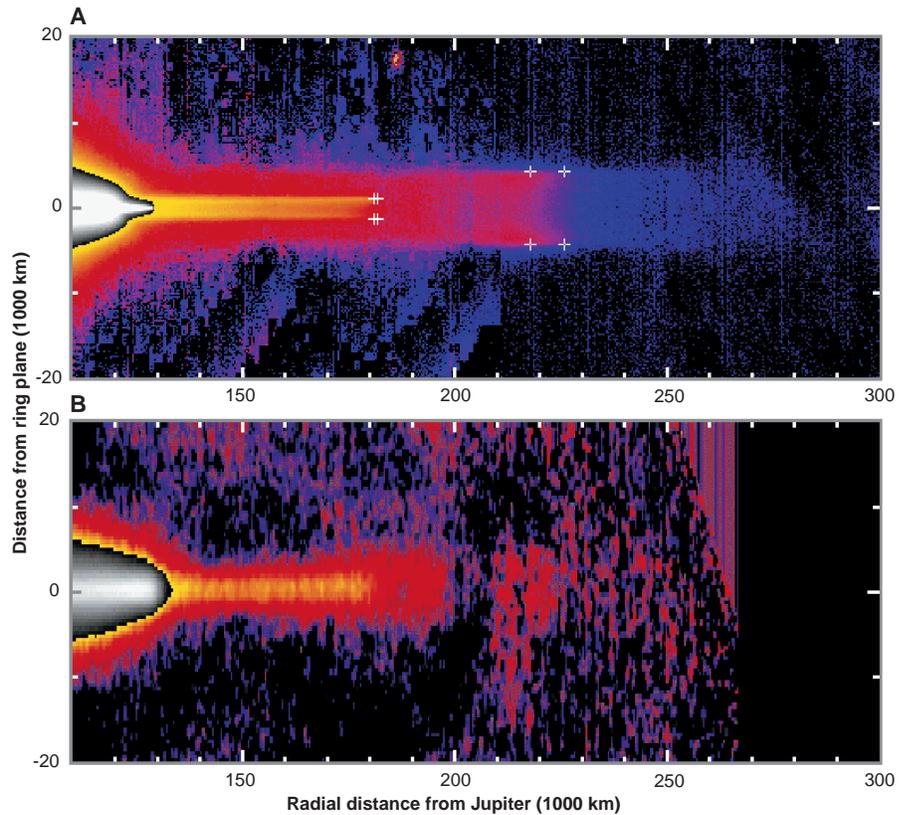

Fig. 1. (**A**) A false-color mosaic of Jupiter's gossamer rings made from four Galileo images (41608-8922, -8968, -9022, and -9045). Images were obtained through the clear filter (central wavelength = 0.611 μm, passband = 0.440 μm) from within Jupiter's shadow (scattering angle θ = 1° to 3°) at an elevation of 0.15°. Images have been reprojected to a common geometric scale of 400 km per pixel radially and 200 km per pixel vertically. The logarithm of the brightness is shown to reduce the dynamic range. In order of increasing brightness, the faint exterior gossamer material is shown in shades of violet, the Thebe ring in blue-red, the Amalthea ring in red-yellow, and the saturated main ring and halo in black and white. Each color change represents roughly a 10-fold increase in brightness. The two gossamer rings have crosses showing the four extremes of the eccentric and inclined motions of Amalthea and Thebe; the full crosses are about 10 times as large as the positional errors of the satellites or ring tips. The top and bottom edges of both gossamer rings are twice as bright as their central cores (5), although this feature is subdued by the logarithmic scale. (**B**) Jupiter's gossamer ring at a back-scattering phase angle of 1.1° taken at 2.27 μm with the Keck 10-m telescope on 14 and 15 August 1997, when Earth's elevation above the ring plane was only 0.17°. The 0.6″ seeing corresponds to a resolution of 1800 km. The main ring, halo, and both gossamer components (the Amalthea ring inward of 181,000 km and, feebly, the Thebe ring inward of 224,000 km) are all apparent; hints of gossamer material are also visible further outward in the Keck data, albeit barely above the noise level, to the frame's edge at ~257,000 km. About 200 individual 20-s frames, from the east and west ansae, were aligned and summed after removing any visible satellites to create this image; later, Jupiter's scattered light was subtracted. The geometric scale and coloring scheme are similar to those of (A).

(1). Resonant charge variation (RCV) (16) may lead to rapid evolution, but its rate is difficult to assess; like plasma drag, it reverses sign at R_{syn}. P-R drag apparently overwhelms plasma drag and RCV because no feature is visible in the Galileo data at R_{syn} (17) and both gossamer rings are located primarily interior to their putative source satellites. This suggests that the ambient plasma density is at least three orders of magnitude less than previously assumed (1). The sputtering time scale should also be increased proportionally, conveniently allowing grains to survive their P-R–driven transit across the ring region.

A particle whose orbit overlaps that of a satellite will strike it eventually. Typical particle lifetimes are ~10 years for zero-inclination grains in the main ring (1). Because inclinations make the problem three dimensional, the collisional lifetimes of grains crossing the orbits of Thebe and Amalthea are longer, ~10^2 to 10^3 years and ~10^4 years for gossamer material that reaches tiny Adrastea. These collisions occur at speeds of order $(e, i)v_{\mathrm{circ}}$ (18) (see Table 1). The main ring grains, having low e and i, strike Metis at velocities $\ll 1$ km s^{-1} and probably are absorbed. Accordingly, the notch in the main ring's brightness surrounding Metis's orbit may reflect the inability of Adrastea debris to transit Metis's path. On the other hand, impacts of Thebe- and Amalthea-derived particles onto Metis and Amalthea occur at ~1 km s^{-1}, raising the possibility of a cascade effect where collisions of Thebe-derived grains into Amalthea produce additional ejecta, which subsequently strike Adrastea and Metis, generating yet more ring material.

The mass of a tenuous ring, assumed to contain particles of a single radius r, is $M_i \sim A\tau\rho r$, where A is the ring's surface area and ρ is the mass density. The masses of the two gossamer rings are each about 10^7 to 10^8 kg if $r = 10$ μm. The main ring and halo will have roughly this mass too, owing to their having much smaller A's but much greater τ's than the gossamer ring.

If the rings are steady-state features, their present-day masses must have been generated in less than $T_{\mathrm{P-R}}$, the time over which material evolves from the system:

$$M_i \lesssim (dM_i/dt)T_{\mathrm{P-R}} \qquad (2)$$

The mass flux density, due to IDPs and interstellar grains, is roughly constant in the outer solar system at 5×10^{-16} kg m^{-2} s^{-1} (19). The impacting particles, moving initially with mean random velocities relative to Jupiter of ~15 km s^{-1}, are gravitationally focused by Jupiter by a factor of two to three. Thus, setting $Y \sim 10^4$, we find that each square centimeter of target produces 10^{-15} kg s^{-1} or erodes at 10^{-5} cm year^{-1} (20). Despite this bombardment, all ring moons have erosional lifetimes that exceed the solar

system's age. Over the ring's P-R lifetime, impacts into Amalthea and Thebe easily generate the mass visible in the rings.

Most ejecta leaves a satellite at ~v_{esc} (21) so that typical orbital eccentricities and inclinations after launch from circular orbits are ~$v_{\mathrm{esc}}/v_{\mathrm{circ}}$ or only 0.003 to 0.005 for Amalthea and Thebe. Therefore, ejecta starts on orbits that are similar to the orbit of the source moon. Because of Jupiter's oblateness and electromagnetic effects, orbital planes precess swiftly (a few months near both Amalthea and Thebe), whereas inclinations are preserved. Thus, after differential precession, grains launched in a single event soon lie on a hoop of height $2a[\sin(i) + (v_{\mathrm{esc}}/v_{\mathrm{circ}})]$ and width $2a[e + (v_{\mathrm{esc}}/v_{\mathrm{circ}})]$. The vertical brightness distribution (Fig. 2) can then be understood with an epicyclic description (22); a hooplike ring is brightest at the turning points of the epicyclic motion, namely, at the top and bottom edges and the outer and inner radial boundaries.

Over times longer than the precession rate, the ejecta evolves inward by P-R drag, so grains from earlier impacts will be nested on hoops nearer to the planet. Viewed from the side, a ring produced steadily over time

in this manner brightens as the LOS approaches the planet (Fig. 2) because the spatial density of grains increases and because the closer LOS also traverses the material on more distant orbits. The precise radial profile will depend on the steadiness of the supply, the nature of the evolution speed, and the birth and death rates of individual grains. The upper and lower edges of the bands will be enhanced over the central core because of the epicyclic effect mentioned above. However, these edges will be less distinct closer to the planet because, with all particles having the same inclination, those on tighter orbits will be less elevated above the midplane.

The ansae of such a ring will have an outward-facing, U-shaped profile; fewer particles will be present near the equatorial outer periphery because epicyclic motions are fastest across this position and, with inward evolution, many orbits no longer extend to the source moons. Eccentricity oscillations due to solar radiation pressure scarcely alter this picture because precession under jovian oblateness limits the oscillation amplitude (23).

The exterior gossamer material does not fit our simple model. Its vertical thickness

Table 1. Dynamical characteristics of Jupiter's ring moons. The orbital elements (semimajor axis a, eccentricity e, and inclination i) are taken from Jet Propulsion Laboratory's JUP120 ephemeris (7). The mean radius R is the cube root of the product of the semiaxes of the triaxial shapes observed by Voyager and Galileo (14). v_{circ} is the satellite's circular orbital velocity around Jupiter. The escape speed v_{esc} is that for an isolated sphere of radius R and density $\rho = 2.0$ g cm^{-3}. v_{max} and v_{min} are the largest and smallest values of the escape velocity, that is, the first speed at which objects thrown at 45° to the surface in the equatorial plane will escape a model ring moon having the measured shape; the v_{min} entry of 0 for Adrastea indicates that some of its surface particles are drawn off by tides.

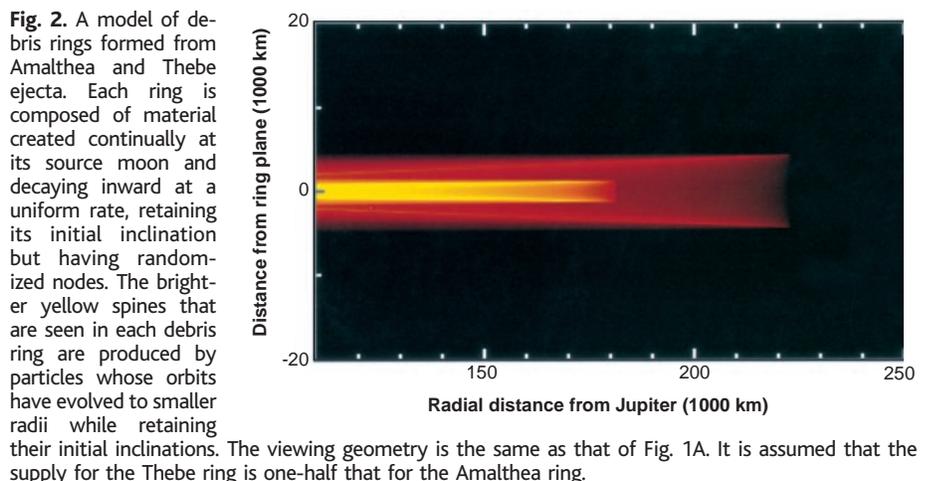|	Metis	Adrastea	Amalthea	Thebe
a (km)	127,945	128,945	181,350	221,900
e	~0.0	~0.0	0.0022	0.0176
i (degrees)	~0.0	~0.0	0.37	1.09
R (km)	21.5	8.2	83.5	49.3
v_{circ} (km s^{-1})	31.5	31.4	26.4	23.9
v_{esc} (m s^{-1})	23	8.7	88	52
v_{max}-v_{min} (m s^{-1})	19–0.5	8.0–0	82–30	45–31

Fig. 2. A model of debris rings formed from Amalthea and Thebe ejecta. Each ring is composed of material created continually at its source moon and decaying inward at a uniform rate, retaining its initial inclination but having randomized nodes. The brighter yellow spines that are seen in each debris ring are produced by particles whose orbits have evolved to smaller radii while retaining their initial inclinations. The viewing geometry is the same as that of Fig. 1A. It is assumed that the supply for the Thebe ring is one-half that for the Amalthea ring.

matches Thebe's inclination, suggesting a dynamical connection. Crude photometry indicates that this material is relatively brighter in the Keck image than in the Galileo data, indicating different photometric properties and therefore different sizes. In contrast, no photometric distinction is apparent between the Thebe and Amalthea rings. However, we have not identified a mechanism that would selectively drive some of Thebe's material inward but other particles outward.

The electrical charge q (1, 24) carried by circumplanetary dust complicates the simple dynamical picture given above. Lorentz forces disturb particle orbits, especially at the locations of Lorentz resonances (25), where the frequencies of electromagnetic perturbations are commensurate with particle epicyclic frequencies (22). Such Lorentz resonances are clustered on either side of R_{syn}, primarily lying within the Amalthea ring. Depending on initial conditions, charge-to-mass ratios, and evolution rates, particles may get captured at such sites (thereby developing large eccentricities or inclinations), may undergo jumps in e or i of varying sign and magnitude, or may pass through unperturbed (26).

Using numerical simulations (23, 26), we followed the orbits of numerous 5- and 50-μm-radius charged dust grains launched from Amalthea and Thebe as they evolve inward toward Jupiter (Fig. 3). The distribution of 50-μm grains is similar to the morphology of the heuristic model described above (Figs. 2 and 3A). Such large grains are relatively unaffected by electromagnetic effects and maintain a nearly constant inclination throughout their evolution toward the planet. In contrast, the electromagnetic perturbations on the 5-μm grains are 10^4 times larger and cause noticeable jumps in i at resonant locations (26) (Fig. 3B). Because gossamer particles presumably have a wide range of sizes, the appearance of the ring will be a weighted sum of images like Fig. 3, A and B, for sizes of all extant particles. The fact that the gossamer rings appear relatively thin (Fig. 1A) implies a limited contribution from small micrometer-sized material relative to larger particles and, if our photometric model is to be accepted, may require a sharp reduction in the ambient charge.

We believe that Adrastea is the primary source of the dust in the main rings because that satellite lies precisely at the main ring's

periphery (5), our calculations show that Adrastea is the most effective supplier of ring material, and the gossamer rings are evidently derived from their associated small moons. Furthermore, in the context of this model, Adrastea's low inclination accounts for the main ring's thinness.

Similarly faint attendant rings, associated with all extant ring moons, should encircle the other giant planets. For the Saturn system, likely sources include Atlas, the F-ring shepherds, the coorbital moons, and the Lagrangian satellites. Indeed, Voyager images do show material present between Saturn's main and F rings (27). The incomplete dust rings that lie in the orbits of Saturn's satellite Pan and Neptune's satellite Galatea may have similar origins.

References and Notes

1. J. A. Burns, M. R. Showalter, G. E. Morfill, in *Planetary Rings*, R. Greenberg and A. Brahic, Eds. (Univ. of Arizona Press, Tucson, AZ, 1984), pp. 200–272; D. A. Mendis *et al.*, in *Saturn*, T. Gehrels and M. S. Matthews, Eds. (Univ. of Arizona Press, Tucson, AZ, 1984), pp. 546–589.
2. L. W. Esposito *et al.*, in *Uranus*, J. T. Bergstralh, E. D. Miner, M. S. Matthews, Eds. (Univ. of Arizona Press, Tucson, AZ, 1991), pp. 410–465; C. C. Porco *et al.*, in *Neptune*, D. P. Cruikshank, Ed. (Univ. of Arizona Press, Tucson, AZ, 1995), pp. 703–804.
3. M. R. Showalter *et al.*, *Icarus* **69**, 458 (1987).
4. M. R. Showalter *et al.*, *Nature* **316**, 526 (1985).
5. M. E. Ockert-Bell *et al.*, *Icarus* **138**, 188 (1999).
6. I. de Pater *et al.*, *ibid.*, p. 214.
7. R. A. Jacobson, personal communication.
8. S. F. Dermott *et al.*, *Nature* **312**, 505 (1984); S. F. Dermott *et al.*, in *Asteroids, Comets, Meteors 1993*, A. Milani, M. di Martino, A. Cellino, Eds. (Kluwer Academic, Dordrecht, Netherlands, 1994), pp. 127–142.
9. Observations of light with wavelength λ made at scattering angle θ highlight particles of radius $r \sim \lambda/2\theta$ (1). Indeed, within the 1.2° to 1.5° range viewed by Galileo, 1-μm particles scatter 10 to 20 times less efficiently than do 5- to 10-μm grains.
10. These calculations assume a constant-size distribution of 30% fractional width. We chose a refractive index corresponding to olivine and pyroxene, but this (and the particle's shape) is unimportant in such a diffraction-dominated regime.
11. E. Grün *et al.*, *Icarus* **62**, 244 (1985).
12. S. J. Weidenschilling *et al.*, in *Planetary Rings*, R. Greenberg and A. Brahic, Eds. (Univ. of Arizona Press, Tucson, AZ, 1984), pp. 367–415; R. M. Canup and L. W. Esposito, *Icarus* **113**, 331 (1995); J. E. Colwell and L. W. Esposito, *J. Geophys. Res.* **98**, 7387 (1993).
13. J. A. Burns *et al.*, *Icarus* **44**, 339 (1980).
14. P. C. Thomas *et al.*, *ibid.* **135**, 360 (1998).
15. The synchronous radius R_{syn} (160,000 km) is the location where a particle's orbital period matches Jupiter's spin period.
16. J. A. Burns and L. Schaffer, *Nature* **337**, 340 (1989); T. G. Northrop, D. A. Mendis, L. E. Schaffer, *Icarus* **79**, 101 (1989).
17. A brightness enhancement at R_{syn}, which was inferred from the Voyager data (4), is not visible in the more sensitive Galileo images; its presence in the Voyager data can be understood in hindsight in terms of the model presented here.
18. D. P. Hamilton and J. A. Burns, *Science* **264**, 550 (1994).
19. J. N. Cuzzi and P. Estrada, *Icarus* **132**, 1 (1998).
20. Because the smallest interplanetary micrometeoroids do not penetrate the jovian magnetosphere, the lifetimes of the tiniest ring grains are set by catastrophic fragmentation rather than erosion (13).
21. P. Farinella *et al.*, *Icarus* **101**, 174 (1993).
22. As seen from a reference frame situated at the mean orbital radius, an orbiting particle approximately traverses an elliptical path ($2ae \times ae$) in a sense opposite to the actual orbital motion while simulta-

Fig. 3. (**A**) The positions of numerous 50-μm radius dust grains after their launch from Amalthea (yellow dots) and Thebe (red dots). The orbits of the particles are subject to Jupiter's gravity (including its oblateness), solar radiation pressure, the electromagnetic force, and P-R drag; the latter two forces are the most important dynamically. Grains are assumed to maintain a constant electric potential of +5 volts (1, 25). The inward drift due to P-R drag was enhanced by a factor of 2500 to allow quicker computations. Because of the existence of an adiabatic invariant, which is conserved during resonance passage, this enhancement does not appreciably affect the behavior of a dust grain at any of the strong resonances discussed here; the effects of some weaker resonances are, however, artificially reduced. These plots have similar viewing geometry to those in Figs. 1 and 2. (**B**) Same as (A), but for 5-μm dust grains; now the P-R drag has been augmented by a factor of 250. The effect of Lorentz resonances on the orbital inclinations of dust grains is noticeable. Amplitudes of the inclination jumps depend sensitively on initial conditions; some Thebe grains, for example, do not get inclination kicks at 160,000 km, whereas many Amalthea grains do.
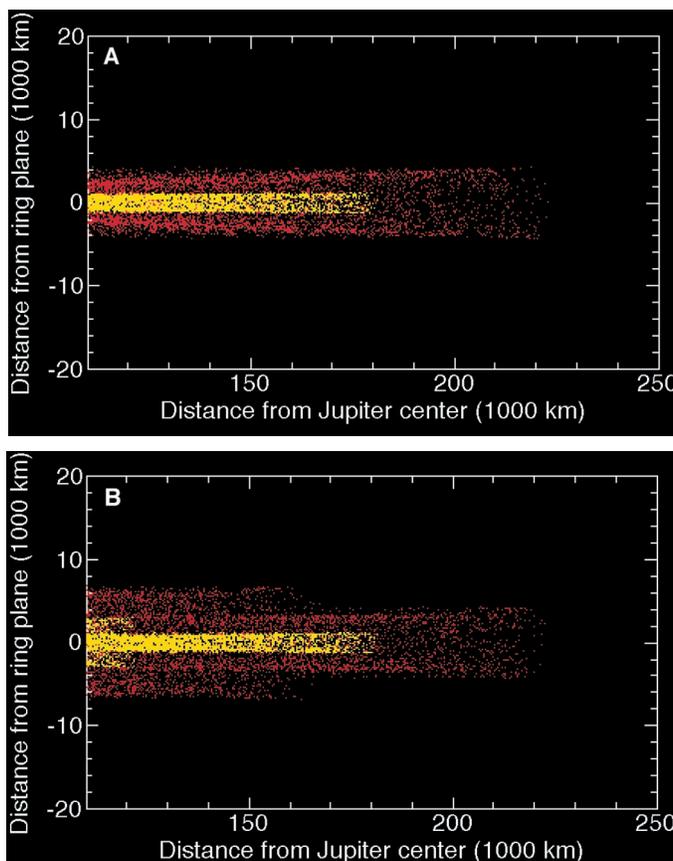
neously oscillating about the equatorial plane by $a[\sin(i)]$. All three excursions—radial, longitudinal, and vertical—occur nearly at the orbital frequency.

23. D. P. Hamilton, *Icarus* **101**, 244 (1993).
24. M. Horanyi, *Annu. Rev. Astron. Astrophys.* **34**, 383 (1996).
25. J. A. Burns *et al.*, *Nature* **316**, 115 (1985).

26. D. P. Hamilton, *Icarus* **109**, 221 (1994); L. Schaffer and J. A. Burns, *ibid.* **96**, 65 (1992).
27. J. A. Burns, J. N. Cuzzi, M. R. Showalter, *Bull. Am. Astron. Soc.* **15**, 1013 (1983); M. R. Showalter, J. A. Burns, D. P. Hamilton, *ibid.* **30**, 1044 (1998); C. D. Murray, M. K. Gordon, S. M. Giuliatti-Winter, *Icarus* **129**, 304 (1997).

28. This research was supported by grants from NASA as well as by the Galileo Project. We acknowledge the help of the Galileo imaging team, especially M. J. S. Belton, J. Veverka, T. V. Johnson, K. Klaasen, and H. Breneman, in obtaining these data.

14 January 1999; accepted 9 April 1999

65,000 Years of Vegetation Change in Central Australia and the Australian Summer Monsoon

B. J. Johnson,[1,2]*† G. H. Miller,[2] M. L. Fogel,[1] J. W. Magee,[3] M. K. Gagan,[4] A. R. Chivas[5]

Carbon isotopes in fossil emu (*Dromaius novaehollandiae*) eggshell from Lake Eyre, South Australia, demonstrate that the relative abundance of C_4 grasses varied substantially during the past 65,000 years. Currently, C_4 grasses are more abundant in regions that are increasingly affected by warm-season precipitation. Thus, an expansion of C_4 grasses likely reflects an increase in the relative effectiveness of the Australian summer monsoon, which controls summer precipitation over Lake Eyre. The data imply that the Australian monsoon was most effective between 45,000 and 65,000 years ago, least effective during the Last Glacial Maximum, and moderately effective during the Holocene.

The Lake Eyre Basin (LEB) extends across one-sixth of Australia's arid and semiarid zones (Fig. 1). Data from lacustrine, fluvial, and eolian deposits within the LEB show that the climate varied during the Quaternary (*1, 2*). These changes exerted a dominant control on vegetation; however, paleovegetation records in the Australian interior are sparse, particularly before 18,000 years ago (18 ka) (*3, 4*). Long-term paleovegetation records for central Australia are important for understanding the interplay between natural climate variability, the arrival of the first human immigrants [~60 ka (*5*)], and the extinction of an element of the Australian megafauna, *Genyornis newtoni* [~50 ka (*6*)]. In our study, we used stable carbon isotopes in emu eggshell (EES) calcite from Lake Eyre, South Australia, to develop a proxy for paleovegetation over the past 65,000 years.

The carbon isotope composition ($\delta^{13}C$) (*7*) of avian eggshell reflects the isotopic composition of the bird's diet integrated over 3 to 5 days (*8*), offset by a biochemical fractionation (*9*). EES carbonate is enriched in ^{13}C by 10 ± 2 per mil relative to the diet (Web Table 1, available at www.sciencemag.org/feature/data/990227.shl). During the egg-laying season [July through September (*10*)], emus are primarily mixed-feeder herbivores, consuming leaves, shoots, fruits, and flowers of trees, shrubs, forbs, and grasses (*11*). Variations in the $\delta^{13}C$ values of EES ($\delta^{13}C_{EES}$) reflect changes in emu diet, which are ultimately driven by changes in the isotopic composition of the flora.

Two isotopically distinct sets of plants dominate the Australian interior: those with C_3 (average $\delta^{13}C = -26.5$ per mil) or those with C_4 (average $\delta^{13}C = -12.5$ per mil) photosynthetic pathways (*12–14*). In Australia, the photosynthetic pathway of grasses depends primarily on the most effective season of rainfall and varies from north to south (*12*). C_3 grasses dominate in regions most affected by winter precipitation (southern Australia), and C_4 grasses become increasingly dominant in regions increasingly affected by summer monsoonal precipitation (central to northern Australia). Almost all of the trees, shrubs, and forbs across Australia are C_3 plants.

We hypothesize that $\delta^{13}C_{EES}$ from Lake Eyre reflects changes in the relative proportion of C_3 to C_4 vegetation and therefore serves as an indirect proxy for the predominant season of rainfall during the past 65 ka. To test this hypothesis, we measured $\delta^{13}C$ in the carbonate fraction of 55 modern EESs from a range of seasonal precipitation and vegetation regimes across Australia (Fig. 1 and Web Table 1). We then compared the $\delta^{13}C$ of modern EES and ambient vegetation with the $\delta^{13}C$ of 219 dated (*15*) fossil EESs from deposits located along the southeastern border of Lake Eyre (Web Table 2, available at www.sciencemag.org/feature/data/990227.shl) (*16*).

The $\delta^{13}C$ values of modern EES mirror the photosynthetic pathways that prevail locally; a pure C_3 signal is found in the south, where all plants (including grasses) use the C_3 pathway, and a mixed C_3-C_4 signal is found in the north as a result of the inclusion
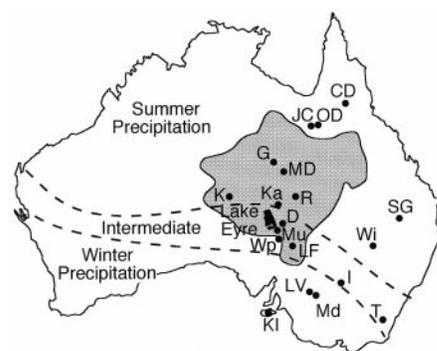
[1]Geophysical Laboratory, Carnegie Institution of Washington, 5251 Broad Branch Road, NW, Washington, DC 20015–1305, USA. [2]Institute of Arctic and Alpine Research and Department of Geological Sciences, University of Colorado, Boulder, CO 80309–0450, USA. [3]Department of Geology, [4]Research School of Earth Sciences, Australian National University, Canberra ACT 0200, Australia. [5]School of Geosciences, University of Wollongong, Wollongong NSW 2522, Australia.

*Present address: School of Oceanography, University of Washington, Seattle, WA 98195–7940, USA.
†To whom correspondence should be addressed. E-mail: bjohnson@ocean.washington.edu

Fig. 1. Map of the Australian mainland and Kangaroo Island (KI), illustrating the locations (solid circles) of sampling sites of modern EES, Lake Eyre, and the Lake Eyre Basin (gray region). Site locations are abbreviated as follows: CD, Carpentaria Downs, QLD; JC, Millungera, QLD; OD, Olga Downs, QLD; G, Glenormiston, QLD; MD, Marion Downs, QLD; K, Kulgera, NT; Ka, Kallakoopah Creek, SA; R, Roseberth, QLD; D, Dulkanina, SA; SG, St. George, QLD; Mu, Muloorina, SA; Wi, Wirrona, NSW; Wp, Wilpoorinna, SA; LF, Lake Froma, SA; I, Ivanhoe, NSW; LV, Lake Victoria, NSW; Md, Mildura, NSW; and T, Tidbinbilla, NSW. Precipitation across northern and central Australia is highly seasonal; the Australian monsoon delivers precipitation to the north during the summer months, and the westerly storm track delivers precipitation to the south during the winter months (*30*). Dashed lines represent the approximate boundaries between the areas influenced primarily by the Australian monsoon and the westerly storm tracks. The intermediate area receives a modicum of precipitation throughout the year.